Climate
of the Past

Monsoon-driven changes in aeolian and fluvial sediment input to the central Red Sea recorded throughout the last 200 000 years

Werner Ehrmann[1], **Paul A. Wilson**[2], **Helge W. Arz**[3], **Hartmut Schulz**[4], and **Gerhard Schmiedl**[5]

[1]Institut für Geophysik und Geologie, Universität Leipzig, Talstraße 35, 04103 Leipzig, Germany
[2]University of Southampton, Waterfront Campus, National Oceanography Centre, Southampton, SO14 3ZH, United Kingdom
[3]Leibniz-Institut für Ostseeforschung, Seestraße 15, 18119 Warnemünde, Germany
[4]Fachbereich Geowissenschaften, Universität Tübingen, Schnarrenbergstraße 94–96, 72076 Tübingen, Germany
[5]Institut für Geologie, Centrum für Erdsystemforschung und Nachhaltigkeit, Universität Hamburg,
Bundesstraße 55, 20146 Hamburg, Germany

Correspondence: Werner Ehrmann (ehrmann@uni-leipzig.de)

Abstract. Climatic and associated hydrological changes controlled the transport processes and composition of the sediments in the central Red Sea during the last ca. 200 kyr. Three different source areas for mineral dust are identified. The dominant source is located in the eastern Sahara (Sudan and southernmost Egypt). We identify its imprint on Red Sea sediments by high smectite and Ti contents, low $^{87}\mathrm{Sr}/^{86}\mathrm{Sr}$, and high $\varepsilon_{\mathrm{Nd}}$. The availability of deflatable sediments was controlled by the intensity of tropical rainfall and vegetation cover over North Africa linked to the African monsoon. Intense dust input to the Red Sea occurred during arid phases, and low input occurred during humid phases. A second, less significant source indicated by palygorskite input is probably located on the eastern Arabian Peninsula and/or Mesopotamia, while the presence of kaolinite suggests an additional minor dust source in northern Egypt. Our grain size data reflect episodes of fluvial sediment discharge to the central Red Sea and document the variable strength in response to all of the precession-paced insolation maxima during our study interval including both those that were strong enough to trigger sapropel formation in the eastern Mediterranean Sea and those that were not. The African humid period most strongly expressed in our Red Sea record was the one during the Eemian last interglacial at ca. 125 ka (when the Baraka River was far more active than today), followed by those at 198, 108, 84, and 6 ka.

1 Introduction

North Africa and the Arabian Peninsula are characterized by strong latitudinal hydrological gradients (e.g. Jolly et al., 1998; Gasse, 2000; Enzel et al., 2015) and feature the largest expanse of hot desert on Earth. The landscape is characterized by large endorheic basins made up of ergs or sand seas such as the Great Sand Sea of the eastern Sahara and the Rub'al Khali covering much of the southern Arabian Peninsula, as well as desert pavements and desiccated alluvial and lacustrine deposits. North Africa is responsible for more than half the global atmospheric load of mineral dust but, together with westernmost Asia, shows marked spatial variability in dust activation frequency (Tegen et al., 2002; Engelstaedter et al., 2006; Stuut et al., 2009; Kumar and Abdullah, 2011; Schepanski et al., 2012; Schepanski, 2018; Kunkelova et al., 2022). Once aloft, dust from North Africa and Arabia can be transported vast distances across the Atlantic and Indian oceans as well as deposited more locally in the Mediterranean Sea, Red Sea, and northern Arabian Sea (e.g. Chester et al., 1977; Sirocko and Lange, 1991; Notaro et al., 2013; Scheuvens et al., 2013; Ramaswamy et al., 2017; Palchan and Torfstein, 2019; Barkley et al., 2021). Properly read, archives of sea-floor sediments that contain windblown dust and riverine material provide a valuable record of change in continental hydroclimate through geological time (e.g. Tiedemann et al., 1994; McGee et al., 2010; Skonieczny et al., 2019). This approach shows that North Africa has a long history of rad-

ical astronomically driven change in hydroclimate, shifting back and forth between arid, dusty conditions and humid, vegetated ones since at least 11 million years ago (Crocker et al., 2022).

Extensive analysis of the late Quaternary geological and archaeological records suggests that, first-order, the pronounced shifts between arid and humid conditions was driven by amplification of seasonal northward migration of the Intertropical Convergence Zone and the tropical rain belt in response to boreal summer insolation maxima driven by the precession of Earth's axis. This resulted in phases of intensified African monsoon circulation and African humid periods (AHPs) (Rossignol-Strick, 1983; Tjallingii et al., 2008; Parton et al., 2015; Grant et al., 2017). During the AHPs, more meteoric water was available, and river systems, wetlands, and lakes existed. The enhanced humidity was associated with a greening of the Sahara and parts of the Arabian Peninsula (e.g. Larrasoaña et al., 2013; Nicholson et al., 2020; Drake et al., 2022). These changes in North African hydrology also triggered sapropel formation in the eastern Mediterranean Sea (e.g. Rohling et al., 2015) via increased freshwater flux down the Nile and the reactivation of ancient northward-draining river systems in Libya (Osborne et al., 2008; Blanchet et al., 2021). The AHPs also led to ecosystem and hydroclimate changes that likely provided temporary pathways for modern human dispersal (e.g. Rosenberg et al., 2011; Coulthard et al., 2013; Timmermann and Friedrich, 2016; Schaebitz et al., 2021; Timmermann et al., 2022). The humid intervals were followed by dry conditions with scarce to no vegetation cover and strong dust transport, comparable to present-day conditions. Proxy records and modelling results indicate that the last five AHPs and their subsequent dust pulses differed in strength, duration, and rate of change, whereby the strongest AHP was associated with the Eemian (Ehrmann et al., 2017; Ehrmann and Schmiedl, 2021; Duque-Villegas et al., 2022). Regional differences are documented for the Holocene AHP, especially a W–E gradient with an earlier but more gradual termination of the AHP in the east and a delayed but more abrupt termination in the west (Renssen et al., 2006; Brovkin and Claussen, 2008; Shanahan et al., 2015; Dallmeyer et al., 2020).

Reconstructions of the late Quaternary hydroclimate of North Africa are mainly built on records from marine sediment cores taken from the North Atlantic Ocean (e.g. deMenocal et al., 2000; Tjallingii et al., 2008; Scheuvens et al., 2013; Tierney et al., 2017) and the eastern Mediterranean Sea (e.g. Larrasoaña et al., 2003; Revel et al., 2010; Bout-Roumazeilles et al., 2013; Ehrmann et al., 2016, 2017; Blanchet et al., 2021; Ehrmann and Schmiedl, 2021). Fewer records are available from the Red Sea (Stein et al., 2007; Palchan et al., 2013; Palchan and Torfstein, 2019; Rojas et al., 2019; Hartman et al., 2020), but its position between the North African and the Arabian deserts makes it an important modern-day sink for mineral dust without the complicating influence of sediment input from large perennial
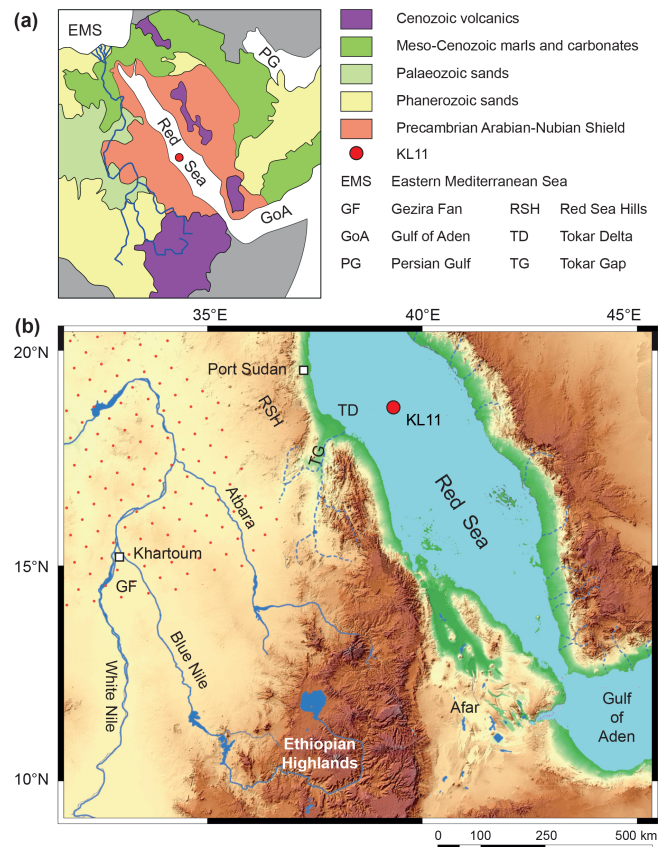

Figure 1. Location of the investigated marine sediment core KL11 in the Red Sea. **(a)** Overview of the Red Sea and the geology of its hinterland (after Stein et al., 2007, and Palchan et al., 2013). **(b)** Topography of the area around the central and southern Red Sea. The main dust source of the Eastern Saharan Potential Source Area (ESPSA) is indicated by hachures (after Kunkelova et al., 2022). Topographic map source: OpenTopoMap (CC-BY-SA).

rivers. These factors, together with its north–south orientation, mean that the Red Sea is well suited to studying meridional change in past hydroclimate in a region where those changes likely exerted a strong control on evolutionary outcomes, including range expansions of our hominid ancestors (e.g. Groucutt et al., 2021; Scerri et al., 2021).

Here we present a sedimentary record from a marine core, KL11, taken from the central Red Sea, spanning the last ca. 210 kyr (Fig. 1). Our records provide a detailed reconstruction of aeolian and fluvial change because our study core was recovered seaward of the Tokar Gap (Fig. 1b), which is a major outlet for North African dust (Hickey and Goudie, 2007), and the Tokar Delta (Trommer et al., 2011), which owes its existence to localized fluvial sediment discharge from Africa during past humid periods by the Baraka River system. We combine high-resolution grain size, clay mineral, and geochemical data together with Nd and Sr isotope data to identify provenance and reconstruct changes in aridity/humidity through time.

2 Materials and methods

We investigated sediment core KL11, which was recovered in 1987 from station M5/2-174/87-KL-2 in the central Red Sea during RV *Meteor* expedition M5/2 (Fig. 1; Nellen et al., 1996; Hemleben et al., 1996; Schmelzer, 1998). The geographic position of the core site is 18°44.5′ N, 39°20.6′ E, and the water depth is 825 m. The recovered section is 21.0 m long, and sediments comprise mainly terrigenous silt with varying amounts of biogenic carbonate, consisting of calcareous nannofossils, foraminifera, and pteropods. The sediments have mostly a greyish, yellowish, or brownish colour. No tephra layers were detected. The core does not show any indications of slumping, debris flows, or turbidites but indicates simple undisturbed "layer-cake" sedimentation. A lithified calcareous interval occurs between 90 and 193 cm depth.

2.1 Chronology

The age model for the upper 901 cm of KL11 was adopted from Hartman et al. (2020). They used the revised age model of Grant et al. (2012), which is based on a comparison of the planktic foraminiferal stable oxygen isotope record of KL11 with the U–Th-dated speleothem record of Soreq cave and integrated eight accelerator mass spectrometry (AMS) radiocarbon ages. The age uncertainties for the upper core interval are defined by the radiometric dating uncertainties, comprising average 2σ errors of ± 0.46 ka for radiocarbon dates (Hartman et al., 2020) and ± 0.84 ka for U–Th dates (Grant et al., 2012). The age model of the interval between 901 and 1105 cm was established by comparison of the smectite record as a proxy for regional monsoon-driven hydrological changes (see below) with the U–Th-dated composite Asian speleothem record (Cheng et al., 2016). Age uncertainties for this core interval are defined by an average 2σ error of ± 2.17 ka for U–Th dates (Wang et al., 2008). Graphical tie points between the KL11 smectite and Asian speleothem $\delta^{18}O$ records comprise 951 cm (179.3 ka), 976 cm (186.5 ka), 1007 cm (191.1 ka), 1054 cm (200.7 ka), 1078 cm (208.7 ka), and 1104 cm (213.2 ka).

In Figs. 2–5 and 7 and Figs. S1–S2 in the Supplement we indicate the timing of the sapropel layers in the eastern Mediterranean Sea that correspond to the AHPs. The ages of sapropels S1–S6 (S1: 5–10.5 ka; S3: 75–81.5 ka; S4: 97–105.5 ka; S5: 121–127 ka; S6: 165–174.5 ka) are taken from Ehrmann and Schmiedl (2021), and the ages of S7 (191–197 ka) and S8 (213–220 ka) come from Emeis et al. (2003). The age models of cores from the eastern Mediterranean Sea are mainly based on a correlation of the $\delta^{18}O$ records to the LR04 stack (Liesicki and Raymo, 2005) and therefore may differ somewhat from the KL11 age model.
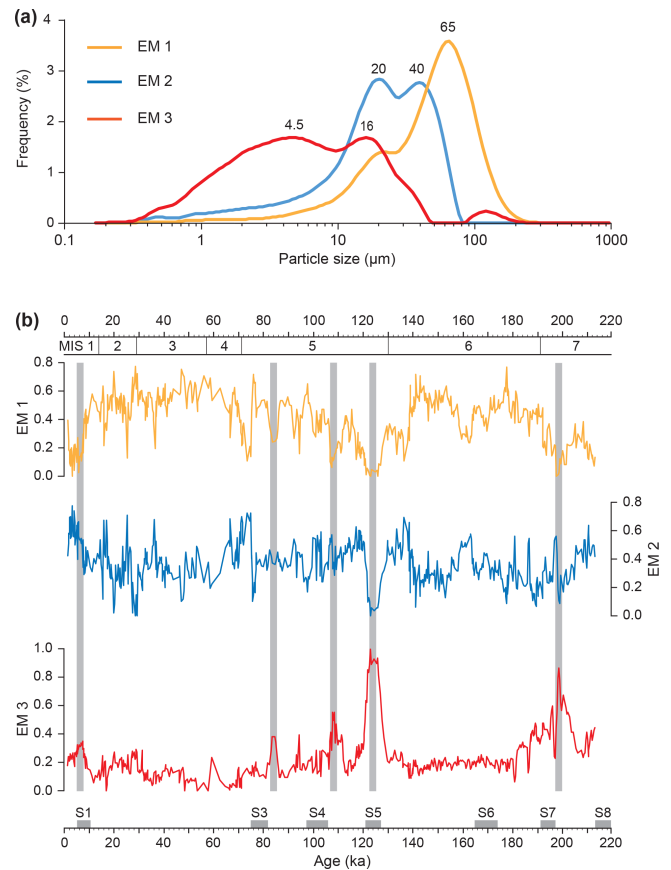

Figure 2. Results of endmember modelling on the grain size distribution of the terrigenous sediment fraction, core KL11. **(a)** Grain size distributions of the three endmembers. The respective modes are given in micrometres. **(b)** Loading patterns of the grain size endmembers. The main peak humid periods as inferred from EM3 are indicated by vertical grey bars. Marine isotope stages (MISs) are indicated at the top; horizontal bars at the bottom indicate sapropel layers S1–S8 in the eastern Mediterranean Sea associated with the African humid periods.

2.2 Grain size, clay mineralogy, and sediment geochemistry

We sampled the upper 1105 cm of core KL11 at 2 cm spacing. The terrigenous components were isolated from bulk sediment by removing carbonate and organic matter with 10 % acetic acid and 5 % hydrogen peroxide, respectively. The terrigenous matter content could be calculated by weight difference because remains of siliceous microfossils were detected only sporadically in the sediments.

Grain size analysis of the terrigenous sediment fraction was performed using a laser particle sizer (Analysette 22, Fritsch GmbH) (Beuscher et al., 2020). We measured 155 size classes within the fraction 0–1000 μm. Concentrations of clay, fine silt, medium silt, coarse silt, and sand were calculated (Fig. S1). The whole range of grain size data were fed into the open-source R-based endmember modelling pro-

gramme RECA (Seidel and Hlawitschka, 2015) to identify similarities and variation patterns within the data set and to group them into subpopulations (endmembers, EMs). We used a convexity error of -6, a weighting exponent of 1, and 1500 iterations for a model with three EMs. This model yields a high r^2 of 0.88 (mean coefficient of determination). Allowing four EMs yields only a minor increase in r^2 to 0.92.

The mineralogical composition of the clay fraction ($< 2\,\mu m$) was investigated by X-ray diffraction (XRD) following standard procedures (Ehrmann and Schmiedl, 2021). Major and trace elements were measured using an ITRAX (Cox Analytical Systems) XRF core scanner at the Leibniz-Institut für Ostseeforschung, Warnemünde, Germany. The scanner was equipped with a Cr tube running at a tube voltage of 30 kV and a tube current of 55 mA. The exposure time was 5 ms per measurement, and the scanning interval was 0.2 cm. No data for calibrating and correcting for the water content were available. No XRF data exist from the calcareous crust. Al, Si, K, Ti, Rb, and Zr were assumed to describe the basic chemical composition of the terrigenous sediment fraction. These elements are reported normalized to total terrigenous element counts by calculating ratios of element counts to total terrigenous element counts (e.g. Ti / terr). Furthermore, the ratio of total terrigenous counts to Ca counts was calculated (Terr / Ca).

2.3   Radiogenic isotopes

All sample processing and analysis were undertaken at the University of Southampton's Waterfront Campus laboratories. The data generated are for the bulk terrigenous fraction (all grain sizes) cleaned to remove contaminating marine phases including barite (see Sect. 2.3.1). This should be borne in mind when comparing our radiogenic isotope data to any of the following: (i) our clay mineralogy data which reflect only the finest grain size fraction, (ii) radiogenic isotope data from grain size sediment splits (there is a well-documented tendency for grain size to exert a secondary influence on Sr isotope data with finer fractions yielding more radiogenic values; see discussions in Bayon et al., 2021, and Jewell et al., 2021), and (iii) samples from marine sediment cores not treated to remove contaminating marine phases (see discussion in Jewell et al., 2022). Briefly, because bedrock geology in our study region ranges from the young basalts of the Ethiopian Highlands to the older continental rocks of the Arabian–Nubian Shield (Fig. 1a), the Sr isotope composition of sources with the potential to contribute sediments to KL11 may lie either above (Arabian–Nubian Shield) or below (Ethiopian Highlands) the value for modern seawater (0.7091). Thus, depending on the identity of the contributing source, uncleaned samples of the terrigenous fraction from the central Red Sea have the potential to yield either artificially low or artificially high Sr isotope values if contaminated by marine phases.

A further past methodological weakness of radiogenic-isotope-based provenance determinations of the terrigenous fraction in marine sediment cores concerns the terrane data used to distinguish different preferential source areas (PSAs). Traditionally, provenance determination has relied on comparison to data sets compiled ad hoc from an array of terrestrial substrates including whole-rock samples, mineral separates, decalcified bulk sediments, non-decalcified bulk sediments, and even fossils. Furthermore, these composites include data from regions with vastly different propensities to produce dust (including regions that produce no dust). For these reasons we compare our data from KL11 to the PSAs of Jewell et al. (2021) and Kunkelova et al. (2022), which were developed using unconsolidated samples collected from actively deflating substrates and for which PSA isotope compositions were determined by applying a weighting factor representing the dust activation frequency of the sampling site.

2.3.1   Isolation of the terrigenous fraction of marine sediments

We treated our samples to remove all authigenic marine contaminants from the isotope fingerprint of the terrigenous fraction (carbonate, authigenic Fe–Mn oxyhydroxide coatings, organic carbon, and marine barite) using the method of Jewell et al. (2022). That study demonstrated that small quantities of marine barite can have a large contaminating effect on the isotopic composition of the terrigenous fraction, especially for Sr. To remove marine barite, samples were leached with 0.2 M diethylene triamine pentaacetic acid (DTPA) in 2.5 M NaOH and left in a water bath set to 80 °C for 30 min. Following the recommended treatment protocol in Jewell et al. (2022), we repeated this step four times on three test samples to determine how many treatments were optimal for complete barite removal at this site. Marine sediments were considered free of marine barite when there was no appreciable decrease in Sr or Ba concentration and no further change in measured $^{87}Sr / ^{86}Sr$ of the silicate fraction with additional DTPA–NaOH treatment. Based on our test samples, we employed one DTPA–NaOH treatment (following the removal of all other marine phases).

2.3.2   Analytical procedure

Our column chemistry procedure followed Jewell et al. (2022). Major element concentrations of sample residues were determined using a Thermo Fisher iCAP6500 dual-view inductively coupled plasma optical emission spectrometer (ICP-OES). Trace element concentrations were measured using a quadrupole inductively coupled plasma mass spectrometer (ICP-MS; Thermo Fisher Scientific XSeries 2). A suite of international rock standards was used for calibration (JB-1a, JGb-1, JB-2, JB-3, BHVO2, AGV-2, BCR-2, BIR-1), plus a spike of 5 ppb In, 5 ppb Re, and 20 ppb Be

as an internal standard. The precision for all measurements was $< 5.6\%$.

2.3.3 Sr isotopes

After column separation, the Sr fraction was dried down and loaded onto an outgassed tantalum filament with 1 mL of a tantalum activator solution. The samples were analysed using a Thermo Fisher Scientific Triton thermal ionization mass spectrometer using a multidynamic procedure and an ^{88}Sr beam of 2 V. Fractionation was corrected using an exponential correction normalized to ^{86}Sr / ^{88}Sr $= 0.1194$. NIST987 was run as a standard in each turret and over the course of this study ^{87}Sr / ^{86}Sr $= 0.710241 \pm 0.000008$ (2 SD, $n = 20$). The long-term average for NIST987 on this instrument is 0.710242 ± 0.000021 (2 SD, $n = 531$).

2.3.4 Nd isotopes

Nd isotope ratios were measured using a multi-collector ICP-MS (MC-ICP-MS; Thermo Fisher Scientific Neptune). Nd isotopic compositions were corrected following the method of Vance and Thirwall (2002) through adjustment to a ^{146}Nd / ^{144}Nd ratio of 0.7219 and a secondary normalization to ^{142}Nd / ^{144}Nd $= 1.141876$. For convenience the Nd isotope ratios are reported in epsilon notation (ε_{Nd}), where ^{143}Nd / ^{144}Nd$_{CHUR}$ represents the Chondrite Uniform Reservoir (CHUR) value of 0.512638 (Jacobsen and Wasserburg, 1980), following Eq. (1):

$$\varepsilon_{Nd} = \left[\frac{^{143}Nd / ^{144}Nd_{sample}}{^{143}Nd / ^{144}Nd_{CHUR}} - 1 \right] \times 10^4. \tag{1}$$

3 Results

The results of our study are presented in Figs. 2–7 and S1–S2. Our sedimentary grain size data show three endmembers (EMs) with distinct modes (Fig. 2). EM1 has a dominant mode in the fine sand fraction at 65 μm and a subordinate shoulder at 20 μm. EM2 is clearly bimodal, with modes in the coarse silt fraction at 40 and 20 μm. EM3 is the finest endmember. It has a mode at 4.5 μm and a second mode at 16 μm. EM1 and EM2 show strongly fluctuating loadings downcore. Both have a distinct minimum around 125 ka, but otherwise they show opposing trends. The loadings of EM3 have a low background level, but distinct maxima occur at about 198, 125, 108, 84, and 6 ka.

The clay mineral assemblage of KL11 is dominated by smectite (Fig. 3). Maxima of about 40 %–50 % occur around 208, 180, 152, 130, 114, 90, 63, 35, and 15 ka. Minima of about 25 %–30 % occur around 196, 166, 142, 128/120, 108, 82, 52, 20, and 6 ka. Illite (15 %–32 %), palygorskite (4 %–13 %), and chlorite (10 %–20 %) show generally similar distribution patterns, opposite to that of smectite. Kaolinite con-
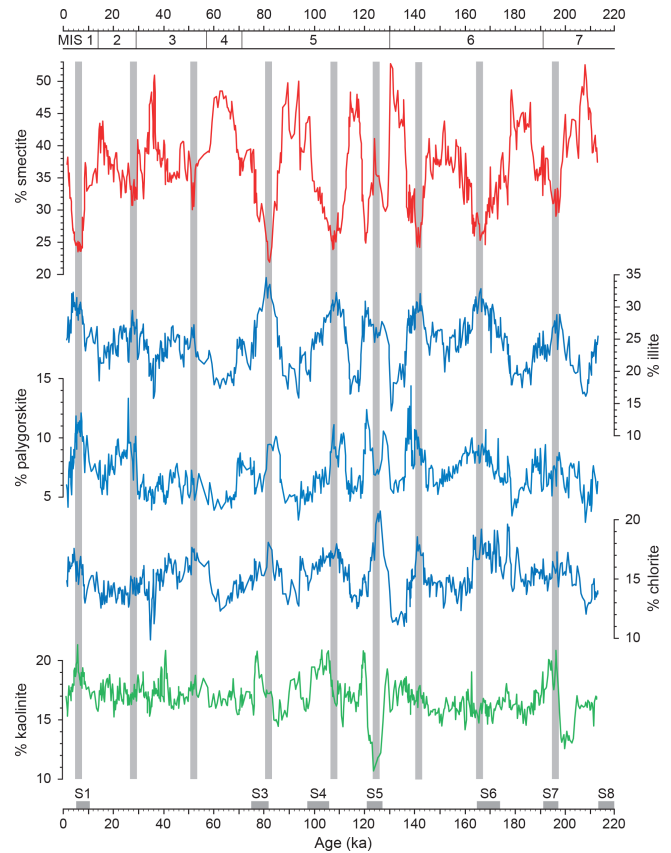

Figure 3. Clay mineral composition of sediments from core KL11. The main peak humid periods as inferred from minima in the smectite concentrations are indicated by vertical grey bars. Marine isotope stages (MISs) are indicated at the top; horizontal bars at the bottom indicate sapropel layers S1–S8 in the eastern Mediterranean Sea associated with the African humid periods.

centrations are relatively uniform at 15 %–20 % but manifest a distinct minimum at ca. 125 ka.

The Ti / terr ratio shows essentially the same temporal distribution pattern as the smectite concentration, while the K / terr ratio exhibits an inverse pattern to those two records (Fig. 4). Terr / Ca correlates well with the concentration of terrigenous matter, which ranges between 20 % and 90 % (Fig. S2). Terr / Ca ratios show substantial millennial-scale variability. Elevated values occur during the glacial periods, and the lowest values occur at ca. 198, 125, 108, 84, and 6 ka.

The radiogenic isotope data on the cleaned bulk terrigenous fraction in samples from KL11 show two main characteristics. First, both ε_{Nd} and ^{87}Sr / ^{86}Sr show a clear coherent structure in their downcore variability (Fig. 5). Second, the neodymium isotope data fall in a narrow range ($\varepsilon_{Nd} \sim -0.5$ to -2.5), and the same is true of the ^{87}Sr / ^{86}Sr isotope data (~ 0.7055 to 0.7075), except for one sample taken from sediments of mid-Eemian age that is distinctly more radiogenic in composition (~ 0.7096).
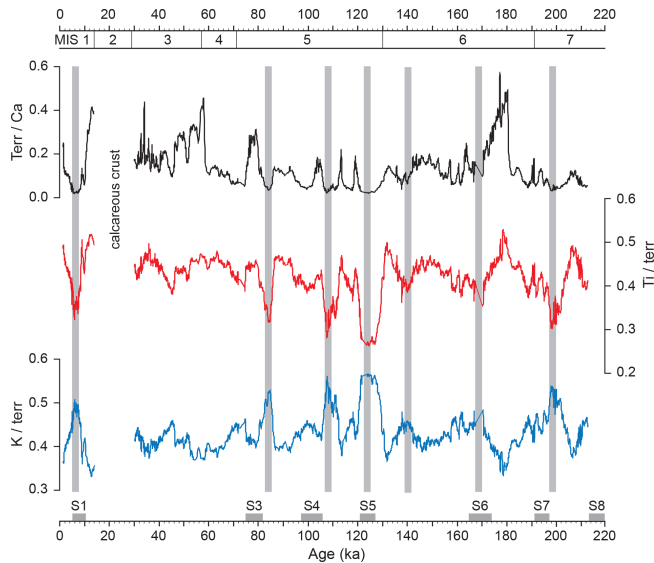
Figure 4. XRF data from core KL11 (five-point running average). Terr / Ca gives the ratio between the sum of terrigenous elements and Ca. Ti and K were normalized by calculating their portion on the terrigenous elements. No data are available from the calcareous crust. The main peak humid periods as inferred from the XRF data are indicated by vertical grey bars. Marine isotope stages (MISs) are indicated at the top; horizontal bars at the bottom indicate sapropel layers S1–S8 in the eastern Mediterranean Sea associated with the African humid periods.
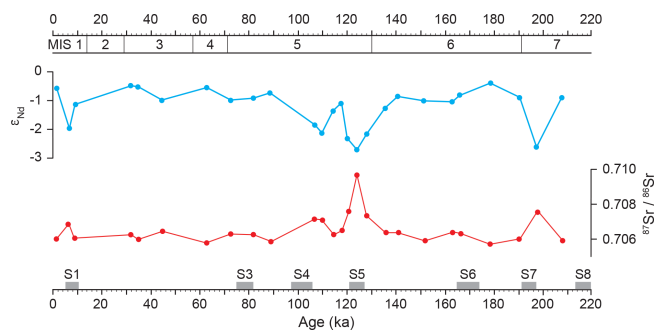
Figure 5. Strontium and neodymium isotope records of the bulk terrigenous fraction in core KL11. Analytical uncertainty in the isotope data is smaller than the size of the data points (see Sect. 2.3). Marine isotope stages (MISs) are indicated at the top; horizontal bars at the bottom indicate sapropel layers S1–S8 in the eastern Mediterranean Sea associated with the African humid periods.

4   Discussion

4.1   Evaluation of proxies for aeolian and fluvial sediment transport to the central Red Sea

The absence of active perennial rivers entering the central Red Sea means that aeolian transport is the main mechanism of sediment delivery to the basin today. Some fluvial sediment discharge is suggested to have occurred during past hu-

mid phases, especially during the Eemian (Arz et al., 2003; Palchan et al., 2013; Hartman et al., 2020).

Both the concentration of terrigenous matter and the Terr / Ca ratios show substantial variability on orbital timescales. Elevated values generally occur during glacial periods (Fig. 4, Fig. S2), and distinct minima occur during the intervals that correspond to the sapropel horizons in the eastern Mediterranean at ca. 198, 125, 108, 84, and 6 ka. However, interpretations of these time series are subject to closed-sum issues because they are affected by fluctuating concentrations of biogenic carbonate as well as changes in terrigenous input. Negative correlations to the abundance of planktic foraminifera and pteropods per gram of dry sediment (Almogi-Labin et al., 1998; Fig. S2) point to elevated carbonate production during interglacial sea-level highstands and concomitant periods of less extreme saline surface waters in the central Red Sea. This implies that carbonate production is a major control of sediment composition. Similar issues complicate the hematite content deduced from magnetic data and the Ti / Ca records that both have been used to quantify the dust accumulation in core KL09, recovered ca. 185 km northwest of KL11 (Roberts et al., 2011; Fig. S2) and showing a similar pattern to our data from KL11.

Detrital grain size (Fig. 2) provides a way to distinguish between aeolian and fluvial transport processes based on the typical modes of the EMs (Beuscher et al., 2017, 2020; Rojas et al., 2019; Blanchet et al., 2021). A mode of 65 μm (EM1) is indicative of coarse dust transported over short distances or by high wind strength. EM2 has modes of 40 μm and 20 μm in the loess grain size fraction and is interpreted as fine-grained dust transported over larger distances or by weaker winds. The interpretation of EM1 and EM2 as dust is supported by the angularity of the coarse silt and sand grains visible under the microscope. We interpret EM3, with a main grain size mode of 4.5 μm, to represent riverine suspension. This endmember also shows a subordinate mode of 16 μm, well in the medium silt grain size range. The distribution of the medium silt displays a rough similarity with the well-correlated fluvial fine silt and clay record (Fig. S1). This may indicate a secondary, more local source of the riverine sediment input. However, a similar mode of 20 μm is present in the aeolian EMs 2 and 3. We therefore infer that fluvial sediment influx was accompanied by a persistent influx of medium silt-sized dust that is responsible, in part, for the 16 μm mode in EM3.

The loadings of EM3 have a low background level, indicating that river discharge to the central Red Sea was a subordinate process through most of our study interval. However, EM3 displays distinct maxima during the monsoonal index maxima associated with AHPs 7, 5, 4, 3, and 1 (Figs. 2b, 7e), documenting intervals of local riverine sediment input. The age discrepancies between the Mediterranean sapropel events and the humid periods reconstructed in this study are probably due to the different age models involved (see Sect. 2.1).

Advection of coarse and fine dust was the dominant process of sediment transport to the central Red Sea during most of the investigated time interval, as indicated by the loadings of the EMs (Fig. 2). The coarse-dust EM1 generally dominated during the glacial intervals and probably indicates stronger wind regimes. Minima in EM1 occur during the humid phases. The influx of coarse dust ceased during AHP7 and AHP5, when fluvial influx was most intense. With the exception of the AHP5 minimum, EM2 loadings show a distribution opposite to EM1.

4.2 Sediment provenance and transport

The different patterns in the temporal distribution of the individual clay minerals, terrigenous elemental ratios, and Nd and Sr isotope data of the KL11 sediments (Figs. 3–5) indicate that several independent source areas contributed to the aeolian and fluvial sediment input to the central Red Sea.

Sources of mineral dust emission surround the Red Sea and are especially intense and proximal to the central Red Sea in the eastern Sahara (Fig. 6a; Kunkelova et al., 2022), including immediately west of Tokar Gap, an approximately 110 km wide lowland pass in the N–S-trending Red Sea Hills, situated at ca. 18° N, some 50 km inland from the Red Sea coast (Fig. 1b). Dust transport through Tokar Gap is especially pronounced during summer (Jiang et al., 2009; Langodan et al., 2014; Kalenderski and Stenchikov, 2016). Wind takes up dust in southernmost Egypt and Sudan (Prospero et al., 2002; Schepanski et al., 2009; Bakker et al., 2019). This area corresponds to the "Potential Source Area 6" (PSA 6) of Scheuvens et al. (2013); the "Eastern North African PSA" of Jewell et al. (2021); or the "Eastern Sahara PSA" of Kunkelova et al. (2022), hereafter referred to as ESPSA. Dust is preferentially activated from desiccated alluvial fans and plains, river beds, lake beds, and wetlands (Tegen et al., 2002; Schepanski et al., 2009), such as the Gezira alluvial fan south of Khartoum. This fan is characterized by presently inactive distributary channels of the Blue Nile and endorheic drainage systems (Williams, 2020).

Sediments in the ESPSA are strongly influenced by weathering products that are derived from the Cenozoic basalts in the Ethiopian Highlands and fluvially transported by the Blue Nile (Padoan et al., 2011; Fig. 1). The isotopic composition of active dust sources in the ESPSA ($\varepsilon_{Nd} \sim -1.1$, $^{87}Sr / ^{86}Sr \sim 0.7059$; Kunkelova et al., 2022; Fig. 6) shows the typical signature of Blue Nile sediments (Palchan et al., 2013). Blue Nile sediments are also characterized by high smectite concentrations derived from weathering of the basaltic material (Hamann et al., 2009; Revel et al., 2014; Ehrmann et al., 2016) and by high Ti contents (Revel et al., 2010; Hennekam et al., 2015). Thus, sediments from the ESPSA can be identified in the central Red Sea by their radiogenic ε_{Nd} and non-radiogenic $^{87}Sr / ^{86}Sr$ signatures, high smectite contents, and high Ti / terr ratios (Figs. 3–6). Some direct wind transport from the Ethiopian Highlands during glacial periods cannot
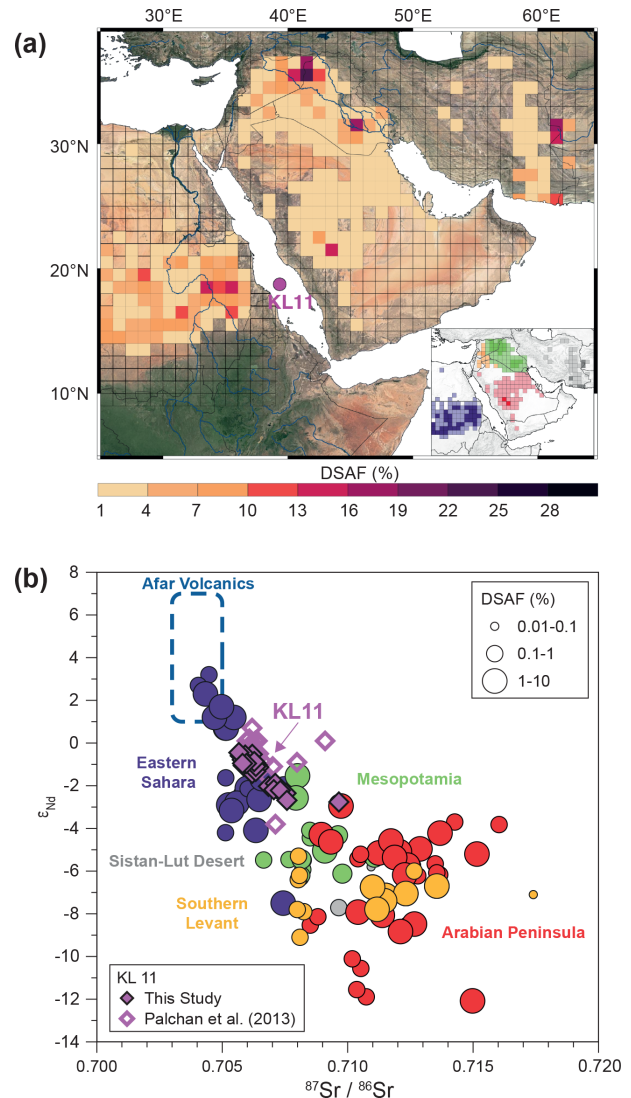

Figure 6. Fingerprinting the provenance and transport pathway of the terrigenous fraction supplied to the central Red Sea (core KL11) using its Sr and Nd isotope composition. **(a)** Dust source activation frequency (DSAF) map of north-east Africa and south-west Asia (calculated as the percentage of days wherein one or more dust events are recorded in a 1° × 1° grid cell; after Kunkelova et al., 2022, and references therein). Background: © Google Earth. Inset shows the preferential dust source areas defined by Kunkelova et al. (2022) colour coded as in panel **(b)**. **(b)** Comparison of Sr and Nd isotope data from core KL11 (pink diamonds) compared to the composition of dust sources (circles). Circle size corresponds to the DSAF **(a)** sampled. Note the strong correspondence between the radiogenic isotope composition of samples from KL11 and the geochemical fingerprint of the eastern Sahara.

be excluded, though the highlands are not dust-active today (Schepanski, 2018; Kunkelova et al., 2022).

Our Nd and Sr isotope data on the cleaned bulk terrigenous fraction from KL11 are so closely aligned with the composition of the ESPSA that, except for the Eemian, they

can be explained by dust from this source alone (Fig. 6b). However, while the high smectite contents in these sediments suggest that the ESPSA is the main source, other clay minerals present suggest there are also contributions from secondary sources. Illite, chlorite, and palygorskite show downcore variability opposite in sign to smectite and Ti / terr (Figs. 3, 4) and point to an additional source area, probably dominated by granitoid and metamorphic rocks and their weathering products. Palygorskite and illite are especially well correlated in our data. Palygorskite is the most diagnostic of these clay minerals. It is a typical wind-blown mineral in sediments of the eastern Mediterranean Sea and a good tracer of Saharan dust. Sources for the eastern Mediterranean palygorskite are Paleogene sedimentary rocks, and their weathering products are located mainly from Tunisia to Egypt (Foucault and Mélières, 2000; Goudie and Middleton, 2001; Bout-Roumazeilles et al., 2007; Scheuvens et al., 2013). However, North Africa is not a likely source of the palygorskite in our records because the aeolian sediments derived from there show a strong negative correlation between palygorskite and illite (Ehrmann and Schmiedl, 2021). Instead we record a positive correlation between these minerals in our downcore record from KL11. The ESPSA in Sudan and the Bodélé depression in Chad can be excluded as sources because, so far, no palygorskite has been reported in dust originating from these sources (Bout-Roumazeilles et al., 2007; Scheuvens et al., 2013).

The Arabian Peninsula is a well-known source of wind-blown palygorskite (Sirocko and Lange, 1991; Sirocko et al., 1991). The Upper Cretaceous and Cenozoic sedimentary rocks, their weathering products, and the soils in eastern and central Saudi Arabia are rich in palygorskite (Aba-Husayn and Sayegh, 1977; Mackenzie et al., 1984; Shadfan et al., 1984; Shadfan and Mashhady, 1985). Palygorskite is also widespread in the flood plains of Mesopotamia (Aqrawi, 1993; Al-Bassam, 2019). Both the lowlands of the eastern Arabian Peninsula and Mesopotamia are major dust emission areas (Hamidi et al., 2013; Jish Prakash et al., 2015; Ramaswamy et al., 2017; Kunkelova et al., 2022) and sources of dust to the Arabian Sea and the Red Sea (Sirocko and Lange, 1991; Notaro et al., 2013; Jish Prakash et al., 2015; Ramaswamy et al., 2017). Our radiogenic isotope data from KL11 are almost entirely distinct from the relatively well-documented (Kunkelova et al., 2022) dust sources of the Arabian Peninsula, the single exception being a sample of Eemian age (Fig. 6b). The isotopic composition of Mesopotamian dust is poorly documented (Kunkelova et al., 2022), but the data available suggest that windblown dust transport from this source may be responsible for the palygorskite deposited at KL11 (Fig. 6). A fluvial origin of palygorskite is unlikely because there are no source and no potential sedimentary source rocks known for this mineral in the small mountainous catchments of the wadis entering the central Red Sea (USGS, 1963; GMRD, 1981). The enhanced palygorskite concentrations correlating with high loadings of the fluvial EM3 are regarded as a dilution effect. As a result of the closed-sum effect, a strong reduction in the concentration of the dominant clay mineral smectite causes an increase in the other clay mineral concentrations.

Kaolinite has a distribution pattern that differs from those of the other clay minerals, requiring a separate source. We infer that this clay mineral is derived from Egypt. High kaolinite concentrations have been reported there in the "Sinai Assemblage" and the "Egyptian Wadi Assemblage"; they originate mainly from Cretaceous and Cenozoic sedimentary rocks (Hamann et al., 2009). Transport is by the NNW winds blowing throughout the year along the axis of the Red Sea to site KL11 (Langodan et al., 2014; Ramaswamy et al., 2017).

Kaolinite is also reported from soils in the western Arabian Peninsula (Aba-Husayn et al., 1980; Shadfan et al., 1984). Derived from such a source, its temporal distribution pattern should be similar to that of palygorskite and illite because the same transport processes would have been responsible for their supply. This, however, is not the case, as kaolinite shows an independent distribution pattern (Fig. 3).

It is likely that illite and chlorite contribute to the fluvial sediment fraction deposited during the humid phases. Illite and chlorite are typical clay minerals derived from physical weathering of granitoid and metamorphic rocks, as they are widespread in the Arabian–Nubian Shield and uplifted terrains on both sides of the central Red Sea (Fig. 1a). The most obvious route for fluvial sediment transport to the central Red Sea is via the Tokar Delta, which is fed by the seasonal Baraka River and its tributaries the Anseba River and Langeb River (Fig. 1b). The Baraka catchment covers some $66\,000\,km^2$. It is active for $40–70\,d\,yr^{-1}$, mainly during autumn, with an annual water discharge of $200–970 \times 10^6\,m^3$ (Trommer et al., 2011). The headwaters in the Red Sea Hills and Eritrean Highland (Hickey and Goudie, 2007) are composed of rocks of the Arabian–Nubian Shield, mainly Precambrian gneisses, schists, and granitoids (GMRD, 1981), and the radiogenic isotope composition of the cleaned bulk terrigenous fraction that we record for the Eemian (Fig. 5) is consistent with a strong imprint of fluvial input to the central Red Sea from these rocks down a reactivated Baraka River. Only small wadis are found on the Arabian side of the central Red Sea. They reach $< 120\,km$ into the peninsula and mainly drain rocks of the Arabian–Nubian Shield and the coastal plain (USGS, 1963), and they are not likely major sources of fluvial sediment influx.

4.3 Climatic forcing of aeolian and fluvial sediment input

Our downcore records are characterized by strong cyclic changes in sediment composition (Figs. 2–5). They document powerful hydrological changes in the hinterland that were caused mainly by precession-driven changes in insolation, the intensity of the African monsoon, and the S–N movement of the tropical rain belt (Fig. 7).
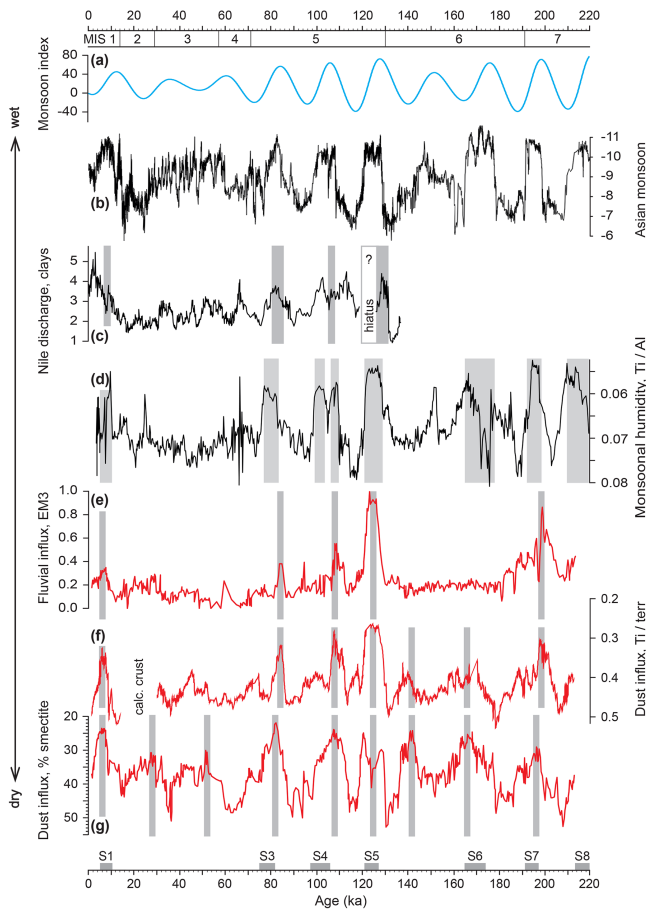
Figure 7. Dry and humid phases of the last ca. 200 kyr. **(a)** Monsoon index (W m^{-2}) relative to present, calculated after Rossignol-Strick (1983) by using the June insolation at 23.45° N and at the Equator (Laskar et al., 2004); **(b)** Asian monsoon (U–Th-dated composite δ^{18}O Asian speleothem record; Cheng et al., 2016); **(c)** Nile discharge as documented by the smectite / (illite + chlorite) ratio in core SL110 off Israel (Ehrmann et al., 2016); **(d)** monsoonal humidity in North Africa as exemplified by Ti / Al ratios in sediments of Ocean Drilling Program (ODP) Site 968, Eratosthenes Seamount, eastern Mediterranean Sea (Konijnendijk et al., 2014); **(e)** fluvial influx to the central Red Sea (KL11, EM3); **(f)** dust influx from the eastern Sahara province to the central Red Sea as documented by Ti / terr in KL11; **(g)** dust influx from the eastern Sahara province to the central Red Sea as documented by the concentration of smectite in KL11. Marine isotope stages (MISs) are indicated at the top; horizontal bars at the bottom indicate sapropel layers S1–S8 in the eastern Mediterranean Sea associated with the African humid periods.

The smectite concentrations and the Ti / terr ratios reflect hydrological changes that controlled the availability of mineral dust in the main source region for the KL11 sediments, the ESPSA. During humid periods, increased summer rainfall and longer wet seasons led to increased chemical weathering of the volcanic rocks in the Ethiopian Highlands, formation of smectite, and high sediment loads down the Blue Nile. The Nile load was partly deposited in the lowlands at the foot of the Ethiopian Highlands, in the ESPSA, and transported in suspension to the Nile Delta (Revel et al., 2010, 2014) and the eastern Mediterranean Sea (Fig. 7c). Hence, smectite maxima occur in sediments deposited beneath the Nile discharge plume off Israel during the AHPs (Ehrmann et al., 2016; Ehrmann and Schmiedl, 2021). Dust emission and aeolian sediment transport from the ESPSA to the central Red Sea were limited during these intervals as marked by minima in smectite concentrations, Ti / terr ratios and ε_{Nd} values, and maxima in ^{87}Sr / ^{86}Sr (Figs. 5, 7f, g). The transport of coarse dust decreased markedly during the AHPs and almost ceased during AHPs 7, 5, and 1, probably due to less strong winds. A severe reduction in the fine-grained dust occurred only during AHP5 (Fig. 2). For AHP1, Palchan and Torfstein (2019) estimated a > 50 % reduction in eastward dust fluxes.

During dry periods, chemical weathering in the Ethiopian Highlands decreased, and less sediment was transported down the Nile (Fig. 7c). Vegetation cover was reduced, and the sediments in the endorheic drainage basins and alluvial plains in the foreland of the Ethiopian Highlands desiccated and became prone to deflation by wind. Dust transport from the ESPSA via Tokar Gap to the central Red Sea became active. Thus, smectite maxima, enhanced Ti / terr ratios, a more radiogenic Nd, and less radiogenic ^{87}Sr / ^{86}Sr compositions are observed in KL11 during dry phases and document active windblown transport. At the same time, dust transport from North Africa to the eastern Mediterranean Sea was enhanced as displayed by the clay mineral record (Ehrmann and Schmiedl, 2021) and by XRF-based elemental ratios, especially Ti / Al, which were also used as a monsoonal humidity index (Fig. 7d; Konijnendijk et al., 2014).

The smectite concentrations of marine sediments in the central Red Sea are especially sensitive recorders of monsoon activity (Fig. 7g). Smectite minima align with the distinct AHPs 1 and 3–7 that were linked to strong insolation maxima and the intense monsoon rains that led to enhanced humidity in North Africa (Fig. 7d) and to sapropel formation in the eastern Mediterranean Sea. They also align with the weaker insolation maxima and less intense humidity during MISs 2, 3, and 6b that did not lead to sapropel formation.

Both the smectite concentrations and Ti / terr record changes in dust influx from the ESPSA. The two records show the same main pattern but differ in detail (Fig. 7f, g). Ti / terr minima are somewhat shorter and sharper than smectite minima during humid periods. This may be due to the heterogeneity of the source. Smectite was measured in the clay fraction, Ti / terr in the bulk sediment. We infer that, during the peak dry phases, both coarse and fine particles were blown out from all areas of the ESPSA. When the climate became more humid, the coarser sediments of the channels, wadis, and alluvial fans of the ESPSA were wetted by surface water and groundwater. They possibly became vegetated and ceased as dust sources. In contrast, the alluvial

plains were still dry and provided smectite-rich dust until the peak humid phase was reached. This interpretation is consistent with the fact that the maxima in the fluvial EM3 and the minima in Ti / terr correlate well with each other. The peaks in these records correlating to AHP3 and AHP7 occur some 2 kyr earlier than the corresponding smectite minima (Fig. 7f, g), presumably signalling wetting of the alluvial plains after their associated fans, channels, and wadis.

The presence of palygorskite (Fig. 3) throughout our record, including in the humid periods, suggests persistent wind transport from Mesopotamia and possibly the Arabian Peninsula (but see Sect. 4.2) to the central Red Sea. According to records from lake sediments, drainage systems, speleothems, and archaeological sites (Armitage et al., 2011; Rosenberg et al., 2011; Drake et al., 2013; Nicholson et al., 2020; Groucutt et al., 2021) and results from climate models (e.g. Dallmeyer et al., 2020, 2021), the Arabian Peninsula was significantly wetter during the humid phases, especially during the Eemian. The rainfall, however, was confined to the summer months. Vegetation expanded particularly in the southern Arabian Peninsula, but desert conditions continued to exist in the northern and north-eastern parts of the Arabian Peninsula (Jennings et al., 2015; Dallmeyer et al., 2020, 2021). In this interpretation, dust uptake was still possible in southern Mesopotamia and northern Arabia, mainly during the dry winter months. However, the fluctuating concentrations of the palygorskite do not allow us to reconstruct the intensity of dust transport because they are influenced by dilution with smectite.

The kaolinite input (Fig. 3), inferred to be sourced from Egypt, is ascribed to north-westerly winds. The concentrations are relatively constant through time. However, a distinct minimum is documented for the pronounced AHP5. It is possible that a southward shift in the Mediterranean winter precipitation system (Kutzbach et al., 2020; Cheddadi et al., 2021) contributed to humidity in the northern Saharan and the Mediterranean regions during AHP5, which would have led to increased vegetation cover and hampered dust uptake.

High loadings of the grain size EM3 (Fig. 7e) suggest fluvial sediment discharge reached KL11 during the AHPs. The maximum of AHP5 is most pronounced, followed by those of AHP7, AHP4, AHP3, and AHP1. The strength of the fluvial sediment discharge signal to the central Red Sea therefore verifies the relative intensities of the individual AHPs as postulated based on records of post-AHP dust pulses to the eastern Mediterranean Sea (Ehrmann et al., 2017; Ehrmann and Schmiedl, 2021) and in the modelling results of Duque-Villegas et al. (2022).

The Eemian (AHP5) maximum in the loadings of the fluvial grain size EM3 correlates well with a secondary maximum in the concentration of smectite, which otherwise is interpreted to be of aeolian origin and derived from the ESPSA (Figs. 2, 3, 7e, 7g). This short and small smectite maximum, however, is probably of fluvial origin. The smectite cannot be provided by the ESPSA via the Baraka River system and the Tokar Delta because the catchment of the rivers does not extend to the ESPSA but is dominated by rocks of the Arabian–Nubian Shield, which do not weather to produce smectite. Basalt occurrences are negligible (GMRD, 1981). Cenozoic volcanic rocks cropping out in the south-western Arabian Peninsula are a possible source of this smectite (Fig. 1a). A number of small wadis originate from this outcrop (USGS, 1963) and may have discharged some volcanic weathering products including smectite during this very intense humid period. Another possible source is the basaltic terrane of the Afar region to the south. Although there are no major rivers draining into the Red Sea or Gulf of Aden today, a palaeodrainage system may have reached the Red Sea during the Eemian. Also, we do not rule out the possibility that extensive rainfall flushed volcanic weathering products to the southern Red Sea, and the fine fraction was transported northwards by marine currents.

AHP6 (ca. 170 ka) finds no expression in the fluvial EM3 (Figs. 2, 7g, S1). This is probably due to the generally cooler glacial boundary conditions with less intense monsoon activity than during interglacial AHPs (Gallego-Torres et al., 2010; Armstrong et al., 2023). The summer rainfalls in the headwaters of the rivers and wadis are inferred to have been too weak to allow the establishment of marked fluvial systems with sediment transport. The diminished smectite concentrations, however, indicate a decline in the dust input from the ESPSA. The humidity was sufficient to hamper dust uptake, possibly by the moistening of the soils and the generation of a vegetation cover. A minimum in the loadings of EM1 indicates a decrease in coarse dust, possibly caused by a reduction in wind strength. A reduction in dust transport during AHP6 is also documented in the eastern Mediterranean Sea (Ehrmann and Schmiedl, 2021).

5 Conclusions

The majority of the terrigenous sediments deposited in the central Red Sea during the last ca. 200 kyr were delivered by aeolian transport. Several source areas probably contributed to the aeolian sediment influx.

The most important dust source was the Eastern Sahara Potential Source Area (ESPSA) of Sudan and southernmost Egypt. It is characterized by volcanic weathering products responsible for high smectite and Ti contents, low ^{87}Sr / ^{86}Sr ratios, and high ε_{Nd} values. A second dust source, less significant according to the radiogenic isotope data, is the eastern Arabian Peninsula and/or Mesopotamia. There, dust sources are rich in palygorskite, illite, chlorite, and K contents. Finally, kaolinite is probably transported as dust from Egypt.

The strength of the African monsoon is strongly imprinted on our record of dust influx from the ESPSA via the Tokar Gap to the central Red Sea. All of the insolation maxima of the last ca. 200 kyr are documented in our records, not only

the strong ones that led to sapropel formation in the eastern Mediterranean Sea.

Fluvial sediment input as indicated by grain size endmember 3 mainly comes via the Tokar Delta from the Baraka catchment.

The intensity of the fluvial influx indicates different strengths of the individual humid periods. Most pronounced was AHP5, followed by AHPs 7, 4, 3, and 1. No fluvial activity is reported for the glacial AHP6. The Baraka River system was sufficiently active during the Eemian to yield a marked radiogenic isotope anomaly in the cleaned bulk terrigenous fraction at KL11.

References

Aba-Husayn, M. M. and Sayegh, A. H.: Mineralogy of Al-Hasa desert soils (Saudi Arabia), Clays Clay Miner., 25, 138–147, https://doi.org/10.1346/CCMN.1977.0250211, 1977.

Aba-Husayn, M. M., Dixon, J. B., and Lee, S. Y.: Mineralogy of Saudi Arabian soils: Southwestern region, Soil Sci. Soc. Am. J., 44, 643–649, https://doi.org/10.2136/sssaj1980.03615995004400030043x, 1980.

Al-Bassam, K. S.: Palygorskite deposits and occurrences in Iraq: an overview, Iraqi Bulletin of Geology and Mining, 9, 203–224, https://ibgm-iq.org/ibgm/index.php/ibgm/article/view/382 (last access: 20 December 2023), 2019.

Almogi-Labin, A., Hemleben, C., and Meischner, D.: Carbonate preservation and climatic changes in the central Red Sea during the last 380 kyr as recorded by pteropods, Mar. Micropaleontol., 33, 87–107, https://doi.org/10.1016/S0377-8398(97)00034-0, 1998.

Aqrawi, A. A. M.: Palygorskite in the recent fluvio-lacustrine and deltaic sediments of southern Mesopotamia, Clay Miner., 28, 153–159, https://doi.org/10.1180/claymin.1993.028.1.15, 1993.

Armitage, S. J., Jasim, S. A., Marks, A. E., Parker, A. G., Usik, V. I., and Uerpmann, H.-P.: The southern route "Out of Africa": Evidence for an early expansion of modern humans into Arabia, Science, 331, 453–456, https://doi.org/10.1126/science.1199113, 2011.

Armstrong, E., Tallavaara, M., Hopcroft, P. O., and Valdes, P. J.: North African humid periods over the past 800,000 years, Nat. Comm., 14, 5549, https://doi.org/10.1038/s41467-023-41219-4, 2023.

Arz, H. W., Lamy, F., Pätzold, J., Müller, P. J., and Prins, M.: Mediterranean moisture source for an Early-Holocene humid period in the northern Red Sea, Science, 300, 118–121, https://doi.org/10.1126/science.1080325, 2003.

Bakker, N. L., Drake, N. A., and Bristow, C. S.: Evaluating the relative importance of northern African mineral dust sources using remote sensing, Atmos. Chem. Phys., 19, 10525–10535, https://doi.org/10.5194/acp-19-10525-2019, 2019.

Barkley, A. E., Olson, N. E., Prospero, J. M., Gatineau, A., Panechou, K., Maynard, N. G., Blackwelder, P., China, S., Ault, A. P., and Gaston, C. J.: Atmospheric transport of North African dust-bearing supermicron freshwater diatoms to South America: Implications for iron transport to the equatorial North Atlantic Ocean, Geophys. Res. Lett., 48, e2020GL090476, https://doi.org/10.1029/2020GL090476, 2021.

Bayon, G., Freslon, N., Germain, Y., Bindeman, I. N., Trinquier, A., and Barrat, J.-A.: A global survey of radiogenic strontium isotopes in river sediments, Chem. Geol., 559, 119958, https://doi.org/10.1016/j.chemgeo.2020.119958, 2021.

Beuscher, S., Krüger, S., Ehrmann, W., Schmiedl, G., Milker, Y., Arz, H., and Schulz, H.: End-member modelling as a tool for climate reconstruction – An Eastern Mediterranean case study, PLoS ONE, 12, e0185136, https://doi.org/10.1371/journal.pone.0185136, 2017.

Beuscher, S., Ehrmann, W., Krüger, S., and Schmiedl, G.: Reconstructing Saharan dust transport to the Eastern Mediterranean Sea during the last 180 ka using endmember modelling of grain size data, Quaternary Res., 94, 156–173, https://doi.org/10.1017/qua.2019.71, 2020.

Blanchet, C. L., Osborne, A. H., Tjallingii, R., Ehrmann, W., Friedrichs, T., Timmermann, A., Brückmann, W., and Frank, M.: Drivers of river reactivation in North Africa during the last glacial cycle, Nat. Geosci., 14, 97–103, https://doi.org/10.1038/s41561-020-00671-3, 2021.

Bout-Roumazeilles, V., Combourieu Nebout, N., Peyron, O., Cortijo, E., Landais, A., and Masson-Delmotte, V.: Connection between South Mediterranean climate and North African atmospheric circulation during the last 50,000 yr BP North Atlantic cold events, Quaternary Sci. Rev., 26, 3197–3215, https://doi.org/10.1016/j.quascirev.2007.07.015, 2007.

Bout-Roumazeilles, V., Combourieu-Nebout, N., Desprat, S., Siani, G., Turon, J.-L., and Essallami, L.: Tracking atmospheric and riverine terrigenous supplies variability during the last glacial and the Holocene in central Mediterranean, Clim. Past, 9, 1065–1087, https://doi.org/10.5194/cp-9-1065-2013, 2013.

Brovkin, V. and Claussen, M.: Comment on "Climate-driven ecosystem succession in the Sahara: The past 6000 years", Science, 322, 1326b, https://doi.org/10.1126/science.1163381, 2008.

Cheddadi, R., Carré, M., Nourelbait, M., François, L., Rhoujjati, A., Manay, R., Ochoa, D., and Schefuß, E.: Early Holocene greening of the Sahara requires Mediterranean winter rainfall, P. Natl. Acad. Sci. USA, 118, e2024898118, https://doi.org/10.1073/pnas.2024898118, 2021.

Cheng, H., Edwards, L., Sinha, A., Spötl, C., Yi, L., Chen, S., Kelly, M., Kathayat, G., Wang, X., Li, X., Kong, X., Wang, Y., Ning, Y., and Zhang, H.: The Asian monsoon over the past 640,000 years and ice age terminations, Nature, 534, 640–646, https://doi.org/10.1038/nature18591, 2016.

Chester, R., Baxter, G. G., Behairy, A. K. A., Connor, K., Cross, D., Elderfield, H., and Padgham, R. C.: Soil-sized eolian dusts from the lower troposphere of the eastern Mediterranean

Sea, Mar. Geol., 24, 201–217, https://doi.org/10.1016/0025-3227(77)90028-7, 1977.

Coulthard, T. J., Ramirez, J. A., Barton, N., Rogerson, M., and Brücher, T.: Were rivers flowing across the Sahara during the Last Interglacial? Implications for human migration through Africa, PLoS ONE, 8, e74834, https://doi.org/10.1371/journal.pone.0074834, 2013.

Crocker, A. J., Naafs, B. D. A., Westerhold, T., James, R. H., Cooper, M. J., Röhl, U., Pancost, R. D., Xuan, C., Osborne, C. P., Beerling, D. J., and Wilson, P. A.: Astronomically controlled aridity in the Sahara since at least 11 million years ago, Nat. Geosci., 15, 671–676, https://doi.org/10.1038/s41561-022-00990-7, 2022.

Dallmeyer, A., Claussen, M., Lorenz, S. J., and Shanahan, T.: The end of the African humid period as seen by a transient comprehensive Earth system model simulation of the last 8000 years, Clim. Past, 16, 117–140, https://doi.org/10.5194/cp-16-117-2020, 2020.

Dallmeyer, A., Claussen, M., Lorenz, S. J., Sigl, M., Toohey, M., and Herzschuh, U.: Holocene vegetation transitions and their climatic drivers in MPI-ESM1.2, Clim. Past, 17, 2481–2513, https://doi.org/10.5194/cp-17-2481-2021, 2021.

deMenocal, P., Ortiz, J., Guilderson, T., and Sarnthein, M.: Coherent high- and low-latitude climate variability during the Holocene warm period, Science, 288, 2198–2202, https://doi.org/10.1126/science.288.5474.2198, 2000.

Drake, N. A., Breeze, P., and Parker, A.: Palaeoclimate in the Saharan and Arabian Deserts during the Middle Palaeolithic and the potential for hominin dispersals, Quatern. Int., 300, 48–61, https://doi.org/10.1016/j.quaint.2012.12.018, 2013.

Drake, N. A., Candy, I., Breeze, P., Armitage, S. J., Gasmi, N., Schwenninger, J. L., Peat, D., and Manning, K.: Sedimentary and geomorphic evidence of Saharan megalakes: A synthesis, Quaternary Sci. Rev., 276, 107318, https://doi.org/10.1016/j.quascirev.2021.107318, 2022.

Duque-Villegas, M., Claussen, M., Brovkin, V., and Kleinen, T.: Effects of orbital forcing, greenhouse gases and ice sheets on Saharan greening in past and future multi-millennia, Clim. Past, 18, 1897–1914, https://doi.org/10.5194/cp-18-1897-2022, 2022.

Ehrmann, W. and Schmiedl, G.: Nature and dynamics of North African humid and dry periods during the last 200,000 years documented in the clay fraction of Eastern Mediterranean deep-sea sediments, Quaternary Sci. Rev., 260, 106925, https://doi.org/10.1016/j.quascirev.2021.106925, 2021.

Ehrmann, W., Schmiedl, G., Seidel, M., Krüger, S., and Schulz, H.: A distal 140 kyr sediment record of Nile discharge and East African monsoon variability, Clim. Past, 12, 713–727, https://doi.org/10.5194/cp-12-713-2016, 2016.

Ehrmann, W., Schmiedl, G., Beuscher, S., and Krüger, S.: Intensity of African Humid Periods estimated from Saharan dust fluxes, PLoS ONE, 12, e0170989, https://doi.org/10.1371/journal.pone.0170989, 2017.

Ehrmann, W., Wilson, P. A., Arz, H. W., Schulz, H., and Schmiedl, G.: Clay mineralogy, grain size, XRF geochemistry and Nd and Sr isotopes from the central Red Sea, PANGAEA [data set], https://doi.org/10.1594/PANGAEA.960352, 2023.

Emeis, K.-C., Schulz, H., Struck, U., Rossignol-Strick, M., Erlenkeuser, H., Howell, M. W., Kroon, D., Mackensen, A., Ishizuka, S., Oba, T., Sakamoto, T., and Koizumi, I.: Eastern

Mediterranean surface water temperatures and $\delta^{18}O$ composition during deposition of sapropels in the late Quaternary, Paleoceanography, 18, 1005, https://doi.org/10.1029/2000PA000617, 2003.

Engelstaedter, S., Tegen, I., and Washington, R.: North African dust emissions and transport, Earth-Sci. Rev., 79, 73–100, https://doi.org/10.1016/j.earscirev.2006.06.004, 2006.

Enzel, Y., Kushnir, Y., and Quade, J.: The middle Holocene climatic records from Arabia: reassessing lacustrine environments, shift of ITCZ in Arabian Sea, and impacts of the southwest Indian and African monsoons, Global Planet. Change, 12, 69–91, https://doi.org/10.1016/j.gloplacha.2015.03.004, 2015.

Foucault, A. and Mélières, F.: Palaeoclimatic cyclicity in central Mediterranean Pliocene sediments: the mineralogical signal, Palaeogeogr. Palaeocl., 158, 311–323, https://doi.org/10.1016/S0031-0182(00)00056-0, 2000.

Gallego-Torres, D., Martinez-Ruiz, F., De Lange, G. J., Jimenez-Espejo, F. J., and Ortega-Huertas, M.: Trace-elemental derived paleoceanographic and paleoclimatic conditions for Pleistocene Eastern Mediterranean sapropels, Palaeogeogr. Palaeocl., 293, 76–89, https://doi.org/10.1016/j.palaeo.2010.05.001, 2010.

Gasse, F.: Hydrological changes in the African tropics since the Last Glacial Maximum, Quaternary Sci. Rev., 19, 189–211, https://doi.org/10.1016/S0277-3791(99)00061-X, 2000.

GMRD (Geological & Mineral Resources Department, Khartoum): Geological Map of the Sudan, 1 : 2,000,000, Paris, https://esdac.jrc.ec.europa.eu/content/geological-map-sudan (last access: 20 December 2023), 1981.

Goudie, A. S. and Middleton, N. J.: Saharan dust storms: nature and consequences, Earth-Sci. Rev., 56, 179–204, https://doi.org/10.1016/S0012-8252(01)00067-8, 2001.

Grant, K. M., Rohling, E. J., Bar-Matthews, M., Ayalon, A., Medina-Elizalde, M., Ramsey, C. B., Satow, C., and Roberts, A. P.: Rapid coupling between ice volume and polar temperature over the past 150,000 years, Nature, 491, 744–747, https://doi.org/10.1038/nature11593, 2012.

Grant, K. M., Rohling, E. J., Westerhold, T., Zabel, M., Heslop, D., Konijnendijk, T., and Lourens, L.: A 3 million year index for North African humidity/aridity and the implication of potential pan-African Humid periods, Quaternary Sci. Rev., 171, 100–118, https://doi.org/10.1016/j.quascirev.2017.07.005, 2017.

Groucutt, H. S., White, T. S., Scerri, E. M. L., Andrieux, E., Clark-Wilson, R., Breeze, P. S., Armitage, S. J., Stewart, M., Drake, N., Louys, J., Price, G. J., Duval, M., Parton, A., Candy, I., Carleton, W. C., Shipton, C., Jennings, R. P., Zahir, M., Blinkhorn, J., Blockley, S., Al-Omari, A., Alsharekh, A. M., and Petraglia, M. D.: Multiple hominin dispersals into Southwest Asia over the past 400,000 years, Nature, 597, 376–380, https://doi.org/10.1038/s41586-021-03863-y, 2021.

Hamann, Y., Ehrmann, W., Schmiedl, G., and Kuhnt, T.: Modern and late Quaternary clay mineral distribution in the area of the SE Mediterranean Sea, Quaternary Res., 71, 453–464, https://doi.org/10.1016/j.yqres.2009.01.001, 2009.

Hamidi, M., Kavianpour, M. R., and Shao, Y.: Synoptic analysis of dust storms in the Middle East, Asia-Pacific J. Atmos. Sci., 49, 279–286, https://doi.org/10.1007/s13143-013-0027-9, 2013.

Hartman, A., Torfstein, A., and Almogi-Labin, A.: Climate swings in the northern Red Sea over the last 150,000 years from εNd and Mg/Ca of marine sediments, Quaternary Sci. Rev., 231, 106205, https://doi.org/10.1016/j.quascirev.2020.106205, 2020.

Hemleben, C, Meischner, D., Zahn, R., Almogi-Labin, A., Erlenkeuser, H., and Hiller, B.: Three hundred eighty thousand year long stable isotope and faunal records from the Red Sea: Influence of global sea level change on hydrography, Paleoceanography, 11, 147–156, https://doi.org/10.1029/95PA03838, 1996.

Hennekam, R., Donders, T. H., Zwiep, K., and de Lange, G. J.: Integral view of Holocene precipitation and vegetation changes in the Nile catchment area as inferred from its delta sediments, Quaternary Sci. Rev., 130, 189–199, https://doi.org/10.1016/j.quascirev.2015.05.031, 2015.

Hickey, B. and Goudie, A. S.: The use of TOMS and MODIS to identify dust storm areas: the Tokar Gap (Sudan) and the Seistan Basin (south west Asia), in: Geomorphological Variations, edited by: Goudie, A. S. and Kalvoda, J., P3K, Prague, 37–57, ISBN 8090358462, 9788090358461, 2007.

Jacobsen, S. B. and Wasserburg, G. J.: Sm-Nd isotopic evolution of chondrites, Earth Planet. Sc. Lett., 50, 139–155, https://doi.org/10.1016/0012-821X(80)90125-9, 1980.

Jennings, R. P., Singarayer, J., Stone, E. J., Krebs-Kanzow, U., Khon, V., Niscancioglu, K. H., Pfeiffer, M., Zhang, X., Parker, A., Parton, A., Groucutt, H. S., White, T. S., Drake, N. A., and Petraglia, M. D.: The greening of Arabia: Multiple opportunities for human occupation of the Arabian Peninsula during the Late Pleistocene inferred from an ensemble of climate model simulations, Quatern. Int., 382, 181–199, https://doi.org/10.1016/j.quaint.2015.01.006, 2015.

Jewell, A. M., Drake, N., Crocker, A. J., Bakker, N. L., Kunkelova, T., Bristow, C. S., Cooper, M. J., Milton, J. A., Breeze, P. S., and Wilson, P. A.: Three North African dust source areas and their geochemical fingerprint, Earth Planet. Sc. Lett., 554, 116645, https://doi.org/10.1016/j.epsl.2020.116645, 2021.

Jewell, A. M., Cooper, M. J., Milton, J. A., James, R. H., Crocker, A. J., and Wilson, P. A.: Chemical isolation and isotopic analysis of terrigenous sediments with emphasis on effective removal of contaminating marine phases including barite, Chem. Geol., 589, 120673, https://doi.org/10.1016/j.chemgeo.2021.120673, 2022.

Jiang, H., Farrar, J. T., Beardsley, R. C., Chen, R., and Chen, C.: Zonal surface wind jets across the Red Sea due to mountain gap forcing along both sides of the Red Sea, Geophys. Res. Lett., 36, L19605, https://doi.org/10.1029/2009GL040008, 2009.

Jish Prakash, P., Stenchikov, G., Kalenderski, S., Osipov, S., and Bangalath, H.: The impact of dust storms on the Arabian Peninsula and the Red Sea, Atmos. Chem. Phys., 15, 199–222, https://doi.org/10.5194/acp-15-199-2015, 2015.

Jolly, D., Harrison, S. P., Damanti, B., and Bonnefille, R.: Simulated climate and biomes of Africa during the Late Quaternary: comparison with pollen and lake status data, Quaternary Sci. Rev., 17, 629–657, https://doi.org/10.1016/S0277-3791(98)00015-8, 1998.

Kalenderski, S. and Stenchikov, G.: High-resolution regional modeling of summertime transport and impact of African dust over the Red Sea and Arabian Peninsula, J. Geophys. Res.-Atmos., 121, 6435–6458, https://doi.org/10.1002/2015JD024480, 2016.

Konijnendijk, T. Y. M., Ziegler, M., and Lourens, L. J.: Chronological constraints on Pleistocene sapropel depositions from high-resolution geochemical records of ODP Sites 967 and

968, Newsl. Stratigr., 47, 263–282, https://doi.org/10.1127/0078-0421/2014/0047, 2014.

Kumar, A. and Abdullah, M. M.: An overview of origin, morphology and distribution of desert forms, sabkhas and playas of the Rub' al Khali Desert of the southern Arabian Peninsula, Earth Sci. India, 4, 105–135, 2011.

Kunkelova, T., Crocker, A. J., Jewell, A. M., Breeze, P. S., Drake, N. A., Cooper, M. J., Milton, J. A., Hennen, M., Shahgedanova, M., Petraglia, M., and Wilson, P. A.: Dust sources in Westernmost Asia have a different geochemical fingerprint to those in the Sahara, Quaternary Sci. Rev., 294, 107717, https://doi.org/10.1016/j.quascirev.2022.107717, 2022.

Kutzbach, J. E., Guan, J., He, F., Cohen, A. S., Orland, I. J., and Chen, G.: African climate response to orbital and glacial forcing in 140,000-y simulation with implications for early modern human environments, P. Natl. Acad. Sci. USA, 117, 2255–2264, https://doi.org/10.1073/pnas.1917673117, 2020.

Langodan, S., Cavaleri, L., Viswanadhapalli, Y., and Hoteit, I.: The Red Sea: A natural laboratory for wind and wave modelling, J. Phys. Oceanogr., 44, 3139–3159, https://doi.org/10.1175/JPO-D-13-0242.1, 2014.

Larrasoaña, J. C., Roberts, A. P., Rohling, E. J., Winklhofer, M., and Wehausen, R.: Three million years of monsoon variability over the northern Sahara, Clim. Dynam., 21, 689–698, https://doi.org/10.1007/s00382-003-0355-z, 2003.

Larrasoaña, J. C., Roberts, A. P., and Rohling, E. J.: Dynamics of green Sahara periods and their role in hominin evolution, PloS ONE, 8, e76514, https://doi.org/10.1371/journal.pone.0076514, 2013.

Laskar, J., Robutel, P., Joutel, F., Gastineau, M., Correia, A. C. M., and Levrard, B.: A long term numerical solution for the insolation quantities of the Earth, Astron. Astrophys., 428, 261–285, https://doi.org/10.1051/0004-6361:20041335, 2004.

Lisiecki, L. E. and Raymo, M. E.: A Pliocene-Pleistocene stack of 57 globally distributed benthic δ^{18}O records, Paleoceanography, 20, PA1003, https://doi.org/10.1029/2004PA001071, 2005.

Mackenzie, R. C., Wilson, M. J., and Mashhady, A. S.: Origin of palygorskite in some soils of the Arabian Peninsula, Dev. Sedimentol., 37, 177–186, https://doi.org/10.1016/S0070-4571(08)70037-2, 1984.

McGee, D., Broecker, W. S., and Winckler, G.: Gustiness: the driver of glacial dustiness?, Quaternary Sci. Rev., 29, 2340–2350, https://doi.org/10.1016/j.quascirev.2010.06.009, 2010.

Nellen, W., Bettac, W., Roether, W., Schnack, D., Thiel, H., Weikert, H., and Zeitzschel, B. (Eds.): MINDIK, Reise Nr. 5, 2 Januar–24 September 1987, Band I. Meteor-Berichte, 96–1, 287 pp., 1996.

Nicholson, S. L., Pike, A. W. G., Hosfield, R., Roberts, N., Sahy, D., Woodhead, J., Cheng, H., Edwards, R. L., Affolter, S., Leuenberger, M., Burns, S. J., Matter, A., and Fleitmann, D.: Pluvial periods in Southern Arabia over the last 1.1 million-years, Quaternary Sci. Rev., 229, 106112, https://doi.org/10.1016/j.quascirev.2019.106112, 2020.

Notaro, M., Alkolibi, F., Fadda, E., and Bakhrjy, F.: Trajectory analysis of Saudi Arabian dust storms, J. Geophys. Res.-Atmos., 118, 6028–6043, https://doi.org/10.1002/jgrd.50346, 2013.

Osborne, A. H., Vance, D., Rohling, E. J., Barton, N., Rogerson, M., and Fello, N.: A humid corridor across the Sahara for the migration of early modern humans out of Africa

120,000 years ago, P. Natl. Acad. Sci. USA, 105, 16444–16447, https://doi.org/10.1073/pnas.0804472105, 2008.

Padoan, M., Garzanti, E., Harlavan, Y., and Villa, I. M.: Tracing Nile sediment sources by Sr and Nd isotope signatures (Uganda, Ethiopia, Sudan), Geochim. Cosmochim. Ac., 75, 3627–3644, http://https://doi.org/10.1016/j.gca.2011.03.042, 2011.

Palchan, D. and Torfstein, A.: A drop in Sahara dust fluxes records the northern limits of the African Humid Period, Nat. Commun., 10, 3803, https://doi.org/10.1038/s41467-019-11701-z, 2019.

Palchan, D., Stein, M., Almogi-Labin, A., Erel, Y., and Goldstein, S. L.: Dust transport and synoptic conditions over the Sahara-Arabia deserts during the MIS6/5 and 2/1 transitions from grain-size, chemical and isotopic properties of Red Sea cores, Earth Planet. Sc. Lett., 382, 125–139, https://doi.org/10.1016/j.epsl.2013.09.013, 2013.

Parton, A., White, T. S., Parker, A. G., Breeze, P. S., Jennings, R., Groucutt, H. S., and Petraglia, M. D.: Orbital-scale climate variability in Arabia as a potential motor for human dispersals, Quatern. Int., 382, 82–97, https://doi.org/10.1016/j.quaint.2015.01.005, 2015.

Prospero, J. M., Ginoux, P., Torres, O., Nicholson, S. E., and Gill, T. E.: Environmental characterization of global sources of atmospheric soil dust identified with the Nimbus 7 Total Ozone Mapping Spectrometer (TOMS) absorbing aerosol product, Rev. Geophys., 40, 1002, https://doi.org/10.1029/2000RG000095, 2002.

Ramaswamy, V., Muraleedharan, P. M., and Prakash Babu, C.: Mid-troposphere transport of Middle-East dust over the Arabian Sea and its effect on rainwater composition and sensitive ecosystems over India, Sci. Rep., 7, 13676, https://doi.org/10.1038/s41598-017-13652-1, 2017.

Renssen, H., Brovkin, V., Fichefet, T., and Goosse, H.: Simulation of the Holocene climate evolution in Northern Africa: The termination of the African Humid Period, Quatern. Int., 150, 95–102, https://doi.org/10.1016/j.quaint.2005.01.001, 2006.

Revel, M., Ducassou, E., Grousset, F. E., Bernasconi, S. M., Migeon, S., Revillon, S., Mascle, J., Murat, A., Zaragosi, S., and Bosch, D.: 100,000 years of African monsoon variability recorded in sediments of the Nile margin, Quaternary Sci. Rev., 29, 1342–1362, https://doi.org/10.1016/j.quascirev.2010.02.006, 2010.

Revel, M., Colin, C., Bernasconi, S., Combourieu-Nebout, N., Ducassou, E., Grousset, F. E., Rolland, Y., Migeon, S., Bosch, D., Brunet, P., Zhao, Y., and Mascle, J.: 21,000 years of Ethiopian African monsoon variability recorded in sediments of the western Nile deep-sea fan, Reg. Environ. Change, 14, 1685–1696, https://doi.org/10.1007/s10113-014-0588-x, 2014.

Roberts, A. P., Rohling, E. J., Grant, K. M., Larrasoaña, J. C., and Liu, Q.: Atmospheric dust variability from Arabia and China over the last 500,000 years, Quaternary Sci. Rev., 30, 3537–3541, https://doi.org/10.1016/j.quascirev.2011.09.007, 2011.

Rohling, E. J., Marino, G., and Grant, K. M.: Mediterranean climate and oceanography, and the periodic development of anoxic events (sapropels), Earth-Sci. Rev., 143, 62–97, https://doi.org/10.1016/j.earscirev.2015.01.008, 2015.

Rojas, V. P., Meynadier, L., Colin, C., Bassinot, F., Valet, J.-P., and Miska, S.: Multi-tracer study of continental erosion and sediment transport to the Red Sea and the Gulf of Aden

during the last 20 ka, Quaternary Sci. Rev., 212, 135–148, https://doi.org/10.1016/j.quascirev.2019.02.033, 2019.

Rosenberg, T. M., Preusser, F., Fleitmann, D., Schwalb, A., Penkman, K., Schmid, T. W., Al-Shanti, M. A., Kadi, K., and Matter, A.: Humid periods in southern Arabia: Windows of opportunity for modern human dispersal, Geology, 39, 1115–1118, https://doi.org/10.1130/G32281.1, 2011.

Rossignol-Strick, M.: African monsoons, an immediate climate response to orbital insolation, Nature, 304, 46–49, https://doi.org/10.1038/304046a0, 1983.

Scerri, E. M. L., Frouin, M., Breeze, P. S., Armitage, S. J., Candy, I., Groucutt, H. S., Drake, N., Parton, A., White, T. S., Alsharekh, A. M., and Petraglia, M. D.: The expansion of Acheulean hominins into the Nefud Desert of Arabia, Sci. Rep., 11, 10111, https://doi.org/10.1038/s41598-021-89489-6, 2021.

Schaebitz, F., Asrat, A., Lamb, H. F., Cohen, A. S., Foerster, V., Duesing, W., Kaboth-Bahr, S., Opitz, S., Viehberg, F. A., Vogelsang, R., Dean, J., Leng, M. J., Junginger, A., Bronk Ramsey, C., Chapot, M. S., Deino, A., Lane, C. S., Roberts, H. M., Vidal, C., Tiedemann, R., and Trauth, M. H.: Hydroclimate changes in eastern Africa over the past 200,000 years may have influenced early human dispersal, Commun. Earth Environ., 2, 123, https://doi.org/10.1038/s43247-021-00195-7, 2021.

Schepanski, K.: Transport of mineral dust and its impact on climate, Geosciences, 8, 151, https://doi.org/10.3390/geosciences8050151, 2018.

Schepanski, K., Tegen, I., Todd, M. C., Heinold, B., Bönisch, G., Laurent, B., and Macke, A.: Meteorological processes forcing Saharan dust emission inferred from MSG-SEVIRI observations of subdaily dust source activation and numerical models, J. Geophys. Res., 114, D10201, https://doi.org/10.1029/2008JD010325, 2009.

Schepanski, K., Tegen, I., and Macke, A.: Comparison of satellite based observations of Saharan dust source areas, Rem. Sens. Environ., 123, 90–97, https://doi.org/10.1016/j.rse.2012.03.019, 2012.

Scheuvens, D., Schütz, L., Kandler, K., Ebert, M., and Weinbruch, S.: Bulk composition of northern African dust and its source sediments – A compilation, Earth-Sci. Rev., 116, 170–194, https://doi.org/10.1016/j.earscirev.2012.08.005, 2013.

Schmelzer, I.: High-frequency event-stratigraphy and paleoceanography of the Red Sea, Dissertation, Universität Tübingen, 124 pp., https://rds-tue.ibs-bw.de/opac/RDSIndex/Search?lookfor=Schmelzer,+Ina&type=AllFields&limit=10&sort=py+desc,+title (last access: 20 December 2023), 1998.

Seidel, M. and Hlawitschka, M.: An R-based function for modeling end member compositions, Math. Geosci., 47, 995–1007, https://doi.org/10.1007/s11004-015-9609-7, 2015.

Shadfan, H. and Mashhady, A. S.: Distribution of palygorskite in sediments and soils of eastern Saudi Arabia, Soil Sci. Soc. Am. J., 49, 243–250, https://doi.org/10.1007/s11004-015-9609-7, 1985.

Shadfan, H., Mashhady, A., Eter, A., and Hussen, A. A.: Mineral composition of selected soils in Saudi Arabia, Z. Pflanzenernaehr. Bodenk., 147, 657–668, https://doi.org/10.1002/jpln.19841470603, 1984.

Shanahan, T. M., McKay, N. P., Hughen, K. A., Overpeck, J. T., Otto-Bliesner, B., Heil, C. W., King, J., Scholz, C. A., and Peck, J.: The time-transgressive termination of the African Humid Period, Nat. Geosci., 8, 140–144, https://doi.org/10.1038/ngeo2329, 2015.

Sirocko, F. and Lange, H.: Clay-mineral accumulation rates in the Arabian Sea during the late Quaternary, Mar. Geol. 97, 105–119, https://doi.org/10.1016/0025-3227(91)90021-U, 1991.

Sirocko, F., Sarnthein, M., Lange, H., and Erlenkeuser, H.: Atmospheric summer circulation and coastal upwelling in the Arabian Sea during the Holocene and the last glaciation, Quaternary Res., 36, 72–93, https://doi.org/10.1016/0033-5894(91)90018-Z, 1991.

Skonieczny, C., McGee, D., Winckler, G., Bory, A., Bradtmiller, L. I., Kinsley, C. W., Polissar, P. J., De Pol-Holz, R., Rossignol, L., and Malaizé, B.: Monsoon-driven Saharan dust variability over the past 240,000 years, Sci. Adv., 5, eaav1887, https://doi.org/10.1126/sciadv.aav1887, 2019.

Stein, M., Almogi-Labin, A., Goldstein, S. L., Hemleben, C., and Starinsky, A.: Late Quaternary changes in desert dust inputs to the Red Sea and Gulf of Aden from 87Sr/86Sr ratios in deep-sea cores, Earth Planet. Sc. Lett., 261, 104–119, https://doi.org/10.1016/j.epsl.2007.06.008, 2007.

Stuut, J.-B., Smalley, I., and O'Hara-Dhand, K.: Aeolian dust in Europe: African sources and European deposits, Quatern. Int., 198, 234–245, https://doi.org/10.1016/j.quaint.2008.10.007, 2009.

Tegen, I., Harrison, S. P., Kohfeld, K., Prentice, C. I., Coe, M., and Heimann, M.: Impact of vegetation and preferential source areas on global dust aerosol: Results from a model study, J. Geophys. Res., 107, 4576, https://doi.org/10.1029/2001JD000963, 2002.

Tiedemann, R., Sarnthein, M., and Shackleton, N. J.: Astronomic timescale for the Pliocene Atlantic δ^{18}O and dust flux records of Ocean Drilling Program Site 659, Paleoceanography, 9, 619–638, https://doi.org/10.1029/94PA00208, 1994.

Timmermann, A. and Friedrich, T.: Late Pleistocene climate drivers of early human migration, Nature, 538, 92–95, https://doi.org/10.1038/nature19365, 2016.

Timmermann, A., Yun, K. S., Raia, P., Ruan, J., Mondanaro, A., Zeller, E., Zollikofer, C., Ponce de León, M., Lemmon, D., Willeit, M., and Ganopolski, A.: Climate effects on archaic human habitats and species successions, Nature, 604, 495–901, https://doi.org/10.1038/s41586-022-04600-9, 2022.

Tierney, J. E., deMenocal, P. B., and Zander, P. D.: A climatic context for the out-of-Africa migration, Geology, 45, 1023–1026, https://doi.org/10.1130/G39457.1, 2017.

Tjallingii, R., Claussen, M., Stuut, J.-B. W., Fohlmeister, J., Jahn, A., Bickert, T., Lamy, F., and Röhl, U.: Coherent high- and low-latitude control of the northwest African hydrological balance, Nat. Geosci., 1, 670–675, https://doi.org/10.1038/ngeo289, 2008.

Trommer, G., Siccha, M., Rohling, E. J., Grant, K., van der Meer, M. T. J., Schouten, S., Baranowski, U., and Kucera, M.: Sensitivity of Red Sea circulation to sea level and insolation forcing during the last interglacial, Clim. Past, 7, 941–955, https://doi.org/10.5194/cp-7-941-2011, 2011.

USGS (United States Geological Survey): Geological Map of the Arabian Peninsula, 1 : 2,000,000, Map I-270A, Washington, D.C., https://nla.gov.au/nla.obj-2458846831/view (last access: 20 December 2023), 1963.

Vance, D. and Thirlwall, M.: An assessment of mass discrimination in MC-ICPMS using Nd isotopes, Chem. Geol., 185, 227–240, https://doi.org/10.1016/S0009-2541(01)00402-8, 2002.

Wang, Y., Cheng, H., Edwards, L., Kong, X., Shao, X., Chen, S., Wu, J., Jiang, X., Wang, X., and An, Z.: Millennial- and orbital-scale changes in the East Asian monsoon over the past 224,000 years, Nature, 451, 1090–1093, https://doi.org/10.1038/nature06692, 2008.

Williams, M.: Water, wind, ice and sea, in: Not just a Corridor. Human Occupation of the Nile Valley and Neighbouring Regions between 75,000 and 15,000 Years ago, edited by: Leplongeon, A., Goder-Goldberger, M., and Pleurdeau, D., Muséum National d'historie Naturelle, Paris, 19–37, ISBN 978-2-85653-931-6, 2020.